CrossMark

Robotic Reverberation Mapping of the Southern Seyfert NGC 3783

Misty C. Bentz[1] ⬡, Rachel Street[2] ⬡, Christopher A. Onken[3] ⬡, and Monica Valluri[4] ⬡
[1] Department of Physics and Astronomy, Georgia State University, Atlanta, GA 30303, USA; bentz@astro.gsu.edu
[2] LCOGT, 6740 Cortona Drive, Suite 102, Goleta, CA 93117, USA
[3] Research School of Astronomy and Astrophysics, Australian National University, Canberra, ACT 2611, Australia
[4] Department of Astronomy, University of Michigan, Ann Arbor, MI 48104, USA

Abstract

We present spectroscopic and photometric monitoring of NGC 3783 conducted throughout the first half of 2020. Time delays between the continuum variations and the response of the broad optical emission lines were clearly detected, and we report reverberation measurements for Hβ, He II λ4686, Hγ, and Hδ. From the time delay in the broad Hβ emission line and the line width in the variable portion of the spectrum, we derive a black hole mass of $M_{\rm BH} = 2.34^{+0.43}_{-0.43} \times 10^7 \, M_\odot$. This is slightly smaller than, but consistent with, previous determinations. However, our significantly improved time sampling ($T_{\rm med} = 1.7$ days compared to $T_{\rm med} = 4.0$ days) has reduced the uncertainties on both the time delay and the derived mass by $\sim$50%. We also detect clear velocity-resolved time delays across the broad Hβ profile, with shorter lags in the line wings and a longer lag in the line core. Future modeling of the full velocity-resolved time-delay response will further improve the reverberation-based mass for NGC 3783, adding it to the small but growing sample of active galactic nuclei for which we have constrained the black hole mass as well as the geometry and kinematics of the broad-ine region. Upcoming MUSE observations at the Very Large Telescope will also allow NGC 3783 to join the smaller sample of black holes where reverberation masses and masses from stellar dynamical modeling may be directly compared.

1. Introduction

Over the last $\sim$25 yr, many studies have led to the understanding that supermassive black holes ($M_{\rm BH} = 10^6$–$10^{10} \, M_\odot$) play a significant role in galaxy evolution and cosmology. The evidence comes from both computational modeling (e.g., Kauffmann & Haehnelt 2000; Granato et al. 2004; Di Matteo et al. 2005; Springel et al. 2005; Hopkins et al. 2006; Ciotti et al. 2010; Scannapieco et al. 2012) and observational results (e.g., Magorrian et al. 1998; Ferrarese & Merritt 2000; Gebhardt et al. 2000; Gültekin et al. 2009; Kormendy & Ho 2013; van den Bosch 2016; Bentz & Manne-Nicholas 2018). Yet, while it is now clear that black holes play an important role in the growth of structure throughout the evolution of our universe, and that this role likely involves feedback from active periods of accretion in the black hole's life, the exact nature and physical manifestations of the symbiotic relationship between galaxies and black holes are not well understood. One key piece to unraveling this mystery rests on an accurate determination of the mass of the central black hole.

Currently, there are only a few methods that are able to directly constrain the gravitational influence of the invisible black hole on luminous tracers (stars or gas) and thus measure $M_{\rm BH}$. In our own galaxy, this has been accomplished with long-term astrometric monitoring of individual stars in the Galactic Center (Genzel et al. 2000; Ghez et al. 2000, 2008). For nearby galaxies ($D \lesssim 100$ Mpc), however, individual stars cannot be resolved in the galactic nuclei, so the most widely used methods instead involve dynamical modeling of the bulk motions of stars or gas (e.g., Macchetto et al. 1997; van der Marel et al. 1998; Barth et al. 2001; Gebhardt et al. 2003). These methods are constrained by the spatial resolution achievable with the current generation of large telescopes and

are thus inherently limited by the distances to the galaxies. In active galaxies, on the other hand, black hole masses are most often derived from reverberation mapping, in which light echoes within the photoionized gas around the black hole are used to measure physical distances that are otherwise spatially unresolvable (Blandford & McKee 1982; Peterson 1993).

Both the dynamical and reverberation techniques currently suffer from several inherent uncertainties and potential systematic biases (see Peterson 2010; Graham et al. 2011; Kormendy & Ho 2013). Both techniques require certain criteria to be fulfilled before they may be applied, which means that, practically speaking, there are few galaxies where $M_{\rm BH}$ may be directly constrained through multiple independent techniques to directly test their consistencies. This is particularly difficult for comparisons of reverberation and stellar dynamical masses: active galaxies with broad emission lines are rare in the local universe, and so almost all galaxies where reverberation mapping may be applied are too distant to achieve the spatial resolution needed to probe the gravitational influence of the black hole on the stellar dynamics.

Dynamical and reverberation mass measurements are critical to our current understanding of galaxy and black hole growth and coevolution. The black hole scaling relationships that are derived from these direct measurements are fundamental for observational studies of black hole mass/luminosity functions as well as cosmological simulations of galaxy evolution. And yet, we do not know if dynamical modeling and reverberation mapping give consistent black hole masses when applied to the same galaxies. The recent highly publicized Event Horizon Telescope results underscored the importance of carrying out black hole mass comparisons by demonstrating that in the case of M87, the black hole mass derived from interferometry agrees

with the stellar dynamical mass but not the gas dynamical mass (Event Horizon Telescope Collaboration et al. 2019).

To date, only two active galactic nuclei (AGNs; NGC 4151 and NGC 3227) have M_{BH} derived from both stellar dynamical modeling and reverberation mapping (Bentz et al. 2006; Davies et al. 2006; Denney et al. 2010; Onken et al. 2014). The mass measurements for NGC 3227 cover a range of approximately an order of magnitude, with the dynamical masses consistently higher than the reverberation masses. On the other hand, the masses for NGC 4151 show reasonable agreement with each other. As one of the nearest ($D \approx 40$ Mpc) and apparently brightest broad-lined Seyferts, NGC 3783 is one of the best candidates for carrying out these important consistency checks.

While NGC 3783 is an obvious candidate for such a study, it currently lacks an Hβ reverberation measurement with the accuracy needed for mass comparisons. NGC 3783 was one of the very first AGNs to be studied through reverberation mapping. This early attempt (Stirpe et al. 1994) employed an image tube as the spectrograph detector, rather than a CCD, and it suffered from linearity problems. Furthermore, the temporal cadence of the spectroscopy was quite low (~once per week) because the broad-line region (BLR) size, and therefore the expected time delay, was not yet well understood. While reprocessing of the initial data set by Onken & Peterson (2002) improved the quality of the reverberation measurements, the median time sampling of 4.0 days, and a few large gaps in coverage leading to an average time sampling of 6.2 days limited the accuracy that could be obtained. Reanalysis of the light curves by Zu et al. (2011) resulted in significantly smaller uncertainties, but ultimately this relies on several assumptions regarding the underlying behavior of the light curves.

We therefore conducted a new monitoring campaign to constrain the optical reverberations in NGC 3783. Our first attempt, using the CTIO 1.5 m telescope in 2012, was unsuccessful because of an extended gap in time coverage in the middle of the campaign due to a scheduling mistake. Our second attempt in 2017 was also unsuccessful because too few spectra were acquired before the observing season for the target had ended. In this paper, we describe the initial results from our third, and finally successful, attempt.

2. Observations

NGC 3783 is an active barred spiral galaxy located at $\alpha = 11{:}39{:}01.7$ and $\delta = -37{:}44{:}19$ with a redshift of $z = 0.0097$. NGC 3783 was monitored photometrically and spectroscopically throughout Semester 2020A with the Las Cumbres Observatory global telescope (LCOGT) network in the Southern Hemisphere (NOAO 2020A-011, PI: Bentz).

2.1. Imaging

V-band photometric monitoring was requested with the Sinistro cameras on the LCOGT network of robotic 1 m telescopes. Images were scheduled to be acquired every ~8 hr beginning in mid-February, but weather and an unexpected and unprecedented global pandemic reduced the time sampling considerably.

Observations began on 2020 February 12 and were initially carried out at Cerro Tololo Inter-American Observatory (CTIO), South African Astronomical Observatory (SAAO), and Siding Spring Observatory (SSO). However, observations
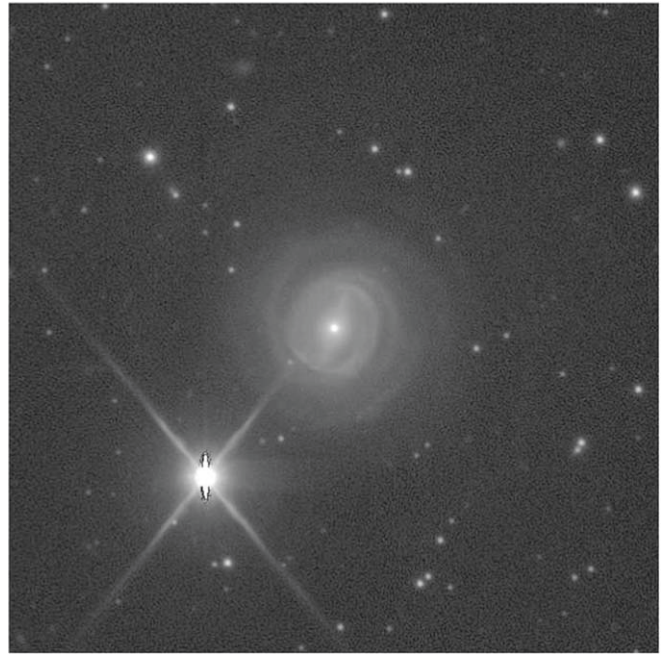

Figure 1. A portion of the reference image of NGC 3783 built from the best individual V-band frames collected throughout the monitoring program. The central $4' \times 4'$ are shown, oriented with north up and east to the left.

were halted at CTIO on 2020 March 18 and at SAAO on 2020 March 26 due to the global spread of the novel coronavirus. While the LCOGT telescopes are robotic, they do require regular maintenance and troubleshooting. CTIO and SAAO, along with most of the major observatories around the world, temporarily suspended all of their mountaintop operations to protect the health and safety of their staff. On 2020 May 6, observations were resumed at SAAO. Observations at SSO continued uninterrupted throughout the semester, and the monitoring program finished as planned at the end of the observing semester on 2020 June 30.

Over the course of the semester, 209 V-band images were acquired: 100 from SSO, 68 from SAAO, and 41 from CTIO. Exposures were set up identically across the observatories, each with an exposure time of 60 s and acquired at a typical airmass of 1.09. The Sinistro cameras have a field of view of $26\!'\!.5 \times 26\!'\!.5$ and an angular sampling of $0\!''\!.389$ pixel^{-1}. The LCOGT pipeline applies typical bias, dark, and flat-field corrections to the raw images and serves up fully reduced images in the archive.

After downloading the reduced images from the archive, we registered all of them to a common reference frame using the SEXTERP package (Siverd et al. 2012). We then employed the image subtraction package ISIS (Alard & Lupton 1998; Alard 2000) to build a reference frame from the best images, convolve the reference frame to match the characteristics of each of the 209 individual images, and then subtract the convolved reference from each image to remove all nonvarying sources. The residual flux in the nucleus of NGC 3783, which is relative to the brightness of the AGN in the reference image (see Figure 1) and may therefore appear as either positive or negative counts, was then measured with aperture photometry.

To convert the residual nuclear flux from counts to calibrated photometry, we modeled the reference frame with GALFIT (Peng et al. 2002, 2010). By constraining the host-galaxy surface brightness features with analytical models, we were
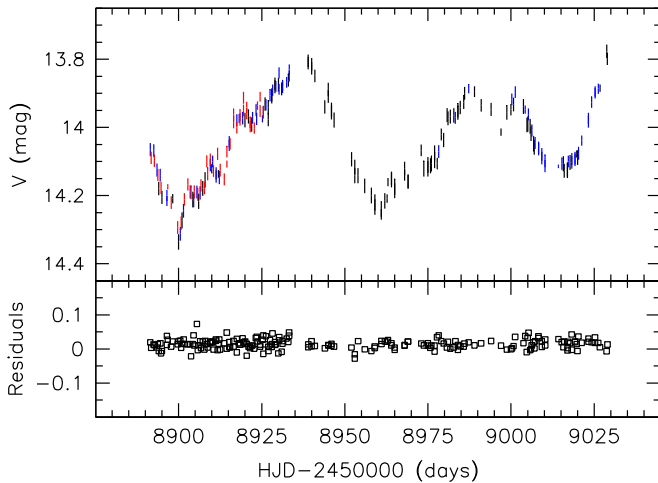
Figure 2. Top: *V*-band photometric light curve of the nuclear emission in NGC 3783. Black points were observed at SSO, blue points were observed at SAAO, and red points were observed at CTIO. Bottom: magnitude residuals after image subtraction for a *V* = 14 mag nonvarying isolated field star.

able to isolate the contribution of the central AGN in the reference image. Using *V*-band measurements of several field stars from the AAVSO Photometric All Sky Survey catalog (Henden & Munari 2014), we determined the magnitude zero point of the reference image, thus defining the conversion from counts to calibrated magnitudes or fluxes for the reference brightness of the AGN. With the reference brightness constrained, the residual fluxes were then calibrated.

Comparison of the measurements from the three observing sites demonstrated that there were slight photometric offsets (on the order of ~0.05–0.10 mag) between the images from SSO, SAAO, and CTIO. The majority of our measurements came from SSO, so we adopted that data set as the photometric anchor. We then determined the best linear fit between measurements from SAAO and SSO that were closely spaced in time ($\lesssim$0.5 day separation), and between closely spaced measurements from CTIO and SSO. Measurements from SAAO and CTIO were then scaled by these best-fit linear relationships to match the SSO measurements.

Finally, the uncertainties on the photometry from image subtraction are known to be underestimated in many cases (e.g., Zebrun et al. 2001; Hartman et al. 2005). We examined the residual counts for nonvarying field stars in the subtracted images and determined the scale factor for the uncertainties that was needed to account for this additional scatter. Our procedure closely followed that of Hartman et al. (2004). The resulting *V*-band light curve is displayed in Figure 2.

Given the strong variability in the nucleus of NGC 3783 over the course of the monitoring program, differential photometry produces a similar *V*-band light curve. However the variations are damped by the host-galaxy flux contribution, and additional noise is introduced through seeing variations that affect the amount of starlight in the photometric aperture. By removing the intrinsically nonvariable host galaxy through image subtraction, we recover the most accurate measurements of the continuum variations that are possible with these data.

2.2. Spectroscopy

Spectra were acquired with the robotic FLOYDS spectrograph on the 2 m Faulkes Telescope South at SSO. FLOYDS is a low-resolution cross-dispersed spectrograph that covers 540–1000 nm in the first order and 320–570 nm in the second order. To minimize the effects of variable seeing on the spectrophotometry, we employed the 6″ slit rotated to a fixed position angle of 0° (N–S orientation) on the sky for all observations. We specifically did not align the slit to the parallactic angle because the strong bar in the host galaxy would then induce a variable host-galaxy contribution in the spectra, making intrinsic nuclear variability more difficult to detect. We limited our observations to airmasses <1.6 so that the use of the 6″ slit would avoid most potential slit losses due to differential refraction at the bluest wavelengths investigated here.

Spectra were scheduled to be acquired every ~24 hr, although weather and oversubscription of the telescope reduced the actual time sampling that was achieved. A total of 50 spectra were obtained, each with an exposure time of 900 s and at a typical airmass of 1.26. The median seeing value during the observations was 2″2. Each observing sequence included HgZn arc lamp images that were taken immediately before and after the science spectrum, as well as a flat-field image.

The LCOGT reduction pipeline applies typical bias, dark, and flat-field corrections; rectifies the two orders of the spectra; and applies rough wavelength and flux calibrations based on a historical wavelength solution and sensitivity function. We downloaded the rectified two-dimensional arc lamp spectra and science spectra from the archive and began our custom reductions with those files. Working in IRAF,[5] we cleaned the science spectra of cosmic rays and then extracted one-dimensional science spectra and arc lamp spectra with an extraction width of 10 pixels. The FLOYDS camera has a pixel scale of 0″337 pixel^{-1}, so the extraction width corresponds to an angular size of 3″37. We then manually identified the arc lamp lines for all 50 visits and applied the updated wavelength solutions to the corresponding science spectra.

We then corrected for small differences between the nightly spectra, including small wavelength shifts, offsets in the flux calibration, and differences in resolution from seeing variations. We applied the van Groningen & Wanders (1992) scaling algorithm, focusing on the [O III] doublet region of the spectra. Each spectrum is compared to a reference spectrum, generally a combination of the best spectra as identified by the user, and the algorithm applies small shifts and smoothing to minimize the differences between the two. In this way, the [O III] emission lines are treated as internal flux calibration sources that are nonvariable on the timescales probed here (see Peterson et al. 2013). Spectra that are treated in this way have been shown by Peterson et al. (1998a) to have relative spectrophotometry that is accurate to ~2% throughout the duration of the monitoring program. Without a similarly strong and unblended emission line in the red spectra, we are unable to properly calibrate the Hα emission region, and so we focused the analysis solely on the blue spectra.

We checked the accuracy of the spectral scaling method by examining the curves of growth for [O III] λ5007, which may be expected to arise from a region that is marginally resolved spatially, and for Hβ, which is dominated by broad emission that arises from a spatially unresolved region. We find that the curves of growth are the same for [O III] and Hβ under the

range of seeing conditions encountered in the monitoring program, with the largest differences occurring at the 1.7% level. Thus, the assumption holds that seeing variations affect measurements of [O III] flux in the same way as the Hβ flux and that these spectra may be intercalibrated at an accuracy that is better than 2% using the [O III] emission lines.

The rough flux calibration determined from the historical sensitivity function does not provide accurate absolute spectrophotometry, however. The typical recommendation for observers is to search the LCOGT archive for standard star spectra that were acquired on the same night as the target spectra; however, the standard star spectra are acquired through a 2″ slit by default and are therefore not suitable for fully calibrating our target spectra, which were acquired through the 6″ slit. Furthermore, measured values of the integrated [O III] λ5007 Å emission-line flux vary over almost an order of magnitude in the literature, from 3.8×10^{-13} erg s^{-1} cm^{-2} (Dopita et al. 2015) on the low end to 1.4×10^{-12} erg s^{-1} cm^{-2} (Ueda et al. 2015) on the high end, even though [O III] fluxes only vary slowly on timescales of years to decades in local Seyferts (e.g., Peterson et al. 2013). An STIS G430M spectrum of NGC 3783 acquired through the 0″.2 slit (GO-12212, PI: Crenshaw) provides an integrated flux of 7.4×10^{-13} erg s^{-1} cm^{-2}. While [O III] imaging of NGC 3783 does show that the emission is quite compact and centered on the nucleus, Fischer et al. (2013) found that faint [O III] emission is still clearly detected out to a radius of ∼2″, and so the flux determined from the STIS spectrum should be taken as a lower limit given the very narrow slit that was employed.

We had previously attempted to carry out this program in early 2017 during a special call for NOAO science to be conducted with LCOGT facilities (NOAO 2017B-0042, PI: Bentz). Scheduling priorities on the 2 m telescope combined with somewhat limited nightly visibility of NGC 3783 based on the time of year led to very poor temporal sampling that did not allow any time delays to be detected. However, as part of that program, we had requested observations of the spectrophotometric standard LTT 4364 through the 6″ slit along with the spectra of NGC 3783, and so we were able to make use of those observations to accurately constrain the integrated flux of the [O III] emission. Starting with the rectified two-dimensional spectra from the pipeline, which have a rough flux calibration from the historical sensitivity function, we extracted the one-dimensional spectra of LTT 4364 and NGC 3783 with the same aperture as above. We then fit a low-order polynomial to the ratio of each observed LTT 4364 spectrum relative to the calibrated spectrum of LTT 4364 from Bessell (1999). The low-order polynomial was then used to correct the shape of the spectrum of NGC 3783 acquired on the same night. Of the 18 nights on which spectra of both targets had been acquired, several were obviously nonphotometric based on the poor quality of the spectra, and so they were discarded. For the remaining 10 nights, we measured the [O III] λ5007 Å flux from the corrected spectra by fitting a local linear continuum under the emission line and integrating the flux above the continuum. One night gave a measurement that was clearly discrepant from the others, so it was discarded. The median of the measurements from the remaining nine nights is $F_{5007} = (10.05 \pm 0.68) \times 10^{-13}$ erg s^{-1} cm^{-2}, which we adopt as the integrated flux of the [O III] λ5007 Å emission line. The final step in processing the 2020 spectra was to scale them to match the adopted [O III] λ5007 Å flux to ensure accuracy in the
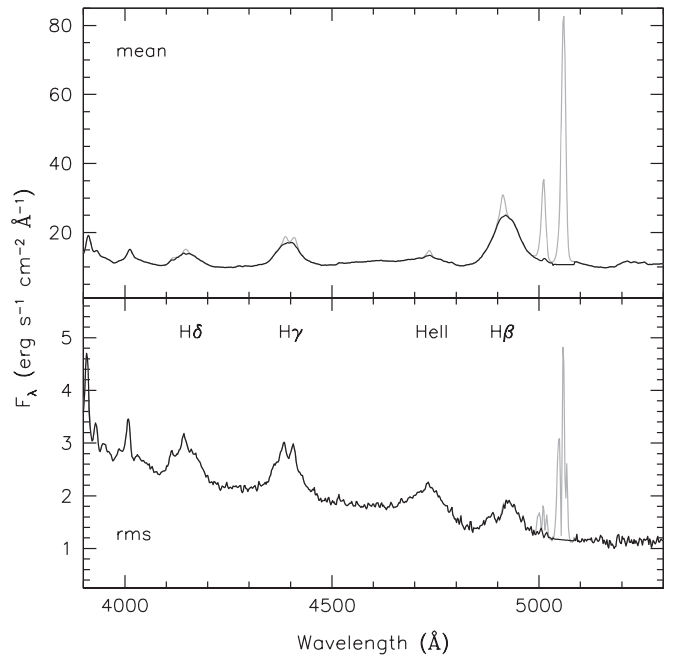

Figure 3. Mean (upper) and rms (lower) of all the blue spectra of NGC 3783 collected throughout the monitoring campaign. Text labels mark the wavelengths for the main broad emission lines in the mean spectrum, with their variable components visible in the rms spectrum. Narrow-line-subtracted spectra are displayed with the black line, while the contributions from several narrow emission lines are displayed in gray.

absolute spectrophotometry. While this step is not important for the reverberation analysis as it does not affect the time delays or emission-line widths, it is vital for determining the AGN luminosity when investigating black hole scaling relationships.

Figure 3 shows the mean and rms of the scaled spectra. The rms spectrum clearly displays strong variability in the broad Balmer emission lines (Hβ, Hγ, and Hδ) as well as the He II λ4686 Å line. There is no discernible variability from Fe II, which appears as a weak emission component in the mean spectrum.

3. Light-curve Analysis

Emission-line light curves were derived from the scaled spectra by fitting a local, linear continuum underneath each emission line of interest and integrating the flux above the continuum. The total flux for each emission line includes the narrow emission-line component, which is simply a constant flux offset. We also measured the continuum flux at $5100 \times (1 + z)$ Å, a region of the spectrum that is free of emission lines and where the host-galaxy contribution is at a local minima.

The V-band and $5100 \times (1 + z)$ Å light curves show a very similar shape, but cover slightly different portions of the time baseline. In particular, the gap in photometric coverage between HJD$-2450000 \approx 8933$–8939 days is partially covered by the $5100 \times (1 + z)$ Å light curve. We therefore scaled the V-band light curve to match the $5100 \times (1 + z)$ Å light curve, based on the linear function that described the relationship between pairs of points that were observed close together in time, and merged them together. In our final continuum light curve, the measurements are binned with 0.25 day bins. All of the light curves that were used for the following analysis are displayed in Figure 4.
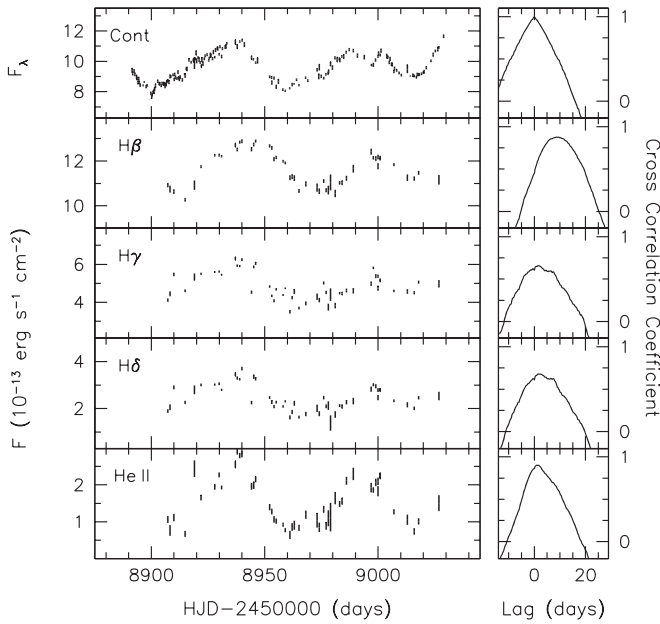
Figure 4. The merged continuum light curve and broad emission-line light curves are displayed in the left panels. The units for the continuum flux density, F_λ, are 10^{-15} erg s^{-1} cm^{-2} Å^{-1}. On the right are the cross-correlation functions relative to the continuum. For the continuum light curve, this is the autocorrelation function. All of the broad emission lines show clear time lags, with Hβ exhibiting the longest lag and He II the shortest.

Common statistics for the light curves are tabulated in Table 1. We list the statistics for the V-band and $5100 \times (1 + z)$ Å light curves separately here, in order to be complete. Column (1) lists the spectral feature, column (2) gives the number of measurements in the light curve, and columns (3) and (4) list the average and median time separation between measurements, respectively. Column (5) gives the mean flux and standard deviation of the light curve, while column (6) lists the mean fractional error. Column (7) lists the excess variance, computed as

$$F_{\mathrm{var}} = \frac{\sqrt{\sigma^2 - \delta^2}}{\langle F \rangle}, \qquad (1)$$

where σ^2 is the variance of the fluxes, δ^2 is their mean-square uncertainty, and $\langle F \rangle$ is the mean flux. Column (8) is the ratio of the maximum to the minimum flux in the light curve.

The variability in the continuum light curve is clearly echoed in the broad emission-line light curves. To quantify the time delays between the variations in the continuum light curve and the variations in an emission line, we first employed the interpolated cross-correlation function (ICCF) method of Gaskell & Sparke (1986) and Gaskell & Peterson (1987) with the modifications of White & Peterson (1994). The ICCF method determines the cross-correlation function (CCF) by averaging together the two CCFs that are calculated when the continuum light curve is interpolated and then when the emission-line light curve is interpolated. The CCFs are displayed in the panels on the right side of Figure 4.

The CCFs may be characterized by the peak value (r_{max}), the time delay at which the peak occurs (τ_{peak}), and the centroid of the CCF (τ_{cent}) near the peak above some value, usually $0.8 r_{\mathrm{max}}$. To quantify the uncertainties on τ_{cent} and τ_{peak}, we employ the Monte Carlo flux randomization/random subset sampling (FR/RSS) method (Peterson et al. 1998b, 2004). The

random subset sampling accounts for the effects of including/excluding any particular data points in the light curves. From a light curve with N data points, N points are selected without regard to whether a point has already been selected. For a point that is selected $1 \leqslant n \leqslant N$ times, the uncertainty on that point is scaled by a factor of $n^{1/2}$, while the typical number of points that are not selected in any specific realization is $\sim 1/e$. The flux randomization then takes the newly sampled light curve and adjusts the flux values of the points randomly with a Gaussian deviation of the flux uncertainty. The CCF of the randomized, sampled light curve is then calculated using the ICCF method and r_{max}, τ_{peak}, and τ_{cent} are recorded. This process is then repeated, and distributions of CCF measurements were built up over 1000 realizations. We take the median of each distribution as the measurement value, and the uncertainties are defined to exclude the upper 15.87% and lower 15.87% of the realizations (corresponding to $\pm 1\sigma$ for a Gaussian distribution). Table 2 lists the observed-frame time delays measured in this way for each broad emission line.

We also constrained the time delays using the `Javelin` package (Zu et al. 2011). `Javelin` fits a damped random walk model to the continuum light curve and then determines the best top-hat model for reprocessing the continuum light curve to match the emission-line light curve. Uncertainties on the model parameters are assessed through a Bayesian Markov Chain Monte Carlo method. `Javelin` is capable of fitting multiple light curves simultaneously, but our initial experiments showed that the results were very sensitive to noise in the light curves. We thus modeled the light curve of each emission line separately with `Javelin`, as we show in Figure 5 for the Hβ emission line, and we report the best-fit observed time delays as τ_{jav} in Table 2.

Finally, we also attempted to constrain the time lags using a different method of treating the spectra. Rather than carefully scaling the nightly spectra using the [O III] lines, we instead measured the equivalent widths of the broad emission lines in each reduced, but unscaled, spectrum. We then multiplied the equivalent widths by the V-band flux measured close in time, or interpolated between measurements when needed, to approximate the calibrated integrated flux of each emission line. While this method has the advantage of not requiring the presence of strong isolated narrow lines and it avoids carrying out the time-intensive scaling step, it assumes that seeing and aperture effects influence the emission lines in the same way as the continuum. For a bright, extended host galaxy like NGC 3783, this assumption may not hold. The resulting light curves for Hβ and He II are similar to, but slightly more noisy than, those in Figure 4 and result in consistent time-delay measurements. The light curves for Hγ and Hδ share the same general shapes as before, but result in time-delay measurements that are longer than those found with the spectral scaling method. Hα produced a noisy light curve, and while the first peak in the continuum light curve was recovered, the subsequent peaks and valleys were lost in the noise. Nevertheless, the recovered time delay was consistent with that measured for Hβ. In the case of Hα, in particular, the varying amount of host-galaxy flux due to seeing effects seems to have detracted from the potential benefits of this method. Similar tests with quasars that have minimal host-galaxy contamination may be more successful.

With the new Hβ time delays determined here, we examined the location of NGC 3783 on the AGN $R_{\mathrm{BLR}}{-}L$ relationship. Following the methods outlined in Bentz et al. (2009, 2013),

Table 1
Light-curve Statistics

Time Series (1)	N (2)	$\langle T \rangle$ (days) (3)	T_{med} (days) (4)	$\langle F \rangle$ (5)	$\langle \sigma_F/F \rangle$ (6)	F_{var} (7)	R_{max} (8)
V	209	0.7 ± 0.8	0.4	9.6 ± 0.9	0.014	0.092	1.536 ± 0.034
5100 Å	50	2.4 ± 2.1	1.7	9.7 ± 1.1	0.020	0.117	1.692 ± 0.069
Hβ	50	2.4 ± 2.1	1.7	11.6 ± 0.7	0.010	0.063	1.255 ± 0.012
He II	50	2.4 ± 2.1	1.7	1.5 ± 0.6	0.085	0.405	4.539 ± 0.777
Hγ	50	2.4 ± 2.1	1.7	4.8 ± 0.7	0.020	0.142	1.802 ± 0.054
Hδ	50	2.4 ± 2.1	1.7	2.4 ± 0.5	0.041	0.215	2.680 ± 0.635

Note. Continuum flux densities (V and 5100 Å) are quoted in units of 10^{-15} erg s^{-1} cm^{-2} Å^{-1} while emission-line fluxes are quoted in units of 10^{-13} erg s^{-1} cm^{-2}.

Table 2
Emission-line Time Lags and Widths

Line	τ_{cent} (days)	τ_{peak} (days)	τ_{jav} (days)	Mean FWHM (km s^{-1})	Mean σ_{line} (km s^{-1})	Rms FWHM (km s^{-1})	Rms σ_{line} (km s^{-1})
Hβ	$9.60^{+0.65}_{-0.72}$	$9.50^{+1.00}_{-1.00}$	$8.64^{+1.71}_{-0.11}$	4486 ± 35	1825 ± 19	4728 ± 676	1619 ± 137
He II	$1.95^{+1.02}_{-0.98}$	$1.50^{+0.50}_{-0.75}$	$1.35^{+0.10}_{-0.08}$	$\cdots$	$\cdots$	4771 ± 638	2146 ± 72
Hγ	$2.66^{+1.35}_{-1.40}$	$2.25^{+2.00}_{-1.25}$	$2.46^{+2.30}_{-0.06}$	4304 ± 79	1621 ± 22	4148 ± 394	1692 ± 36
Hδ	$3.39^{+1.17}_{-1.29}$	$3.00^{+2.00}_{-1.75}$	$4.76^{+0.04}_{-2.31}$	4274 ± 100	1611 ± 30	4035 ± 461	1709 ± 49

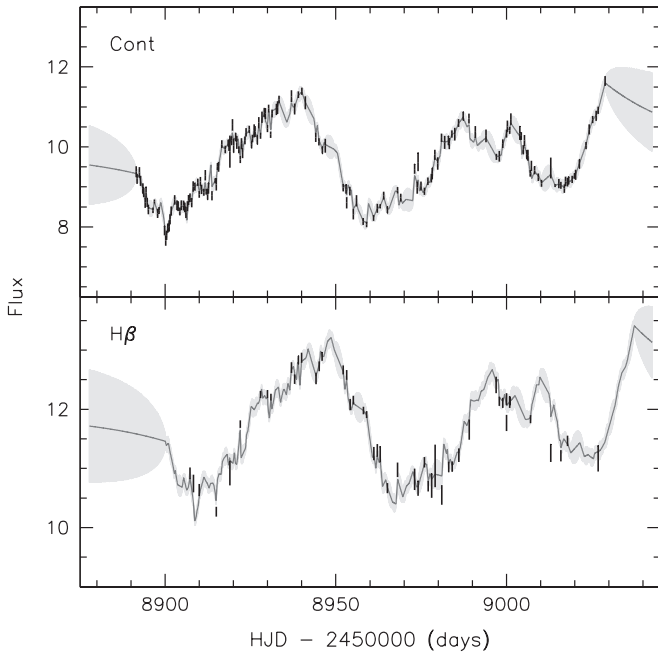**Note.** Time lags are listed as measurements in the observer's frame.

Figure 5. Continuum and Hβ light curves (data points) with the mean `Javelin` model light curves (solid lines) and uncertainties (gray shaded regions) overlaid. The uncertainties on the models were derived from the standard deviation of the individual realizations.

we estimated the host-galaxy contribution to the 5100 Å flux from a high-resolution Hubble Space Telescope image of NGC 3783, finding $f_{\mathrm{gal}} = (2.76 \pm 0.28) \times 10^{-15}$ erg s^{-1} cm^{-2} Å^{-1}, approximately 28% of the continuum flux during the monitoring campaign. The luminosity distance to NGC 3783 is $\sim$42 Mpc, which is well within the volume where peculiar velocities may be problematic. Kourkchi & Tully (2017) assigned NGC 3783 to a group of nine galaxies, only two of which have distance

measurements, and report a group-averaged distance of 42 ± 6 Mpc. After correcting for the starlight contribution to the continuum flux and adopting a distance of 42 Mpc, we find a nuclear luminosity of log $\lambda L_{5100} = 43.02 \pm 0.02$ erg s^{-1}. The best fit to the $R_{\mathrm{BLR}}-L$ relationship reported by Bentz et al. (2013) predicts an Hβ time delay of 10.1 ± 1.8 days for the luminosity of NGC 3783, which agrees well with the time delay reported here.

4. Emission-line Widths

The width of a broad line gives an estimate of the line-of-sight velocity of gas in the BLR. Many previous reverberation experiments have shown that the typical velocities of the BLR gas that responds to continuum variations, the rms line profiles, may not be the same as those measured from the integrated line emission (the mean line profiles). Furthermore, the narrow emission is blended with the broad emission in the spectra but is emitted from a physically distinct region with different kinematics. For these reasons, the line widths measured in the rms spectrum are generally preferred, as they correspond only to gas that reverberates. Furthermore, the second moment of the line profile, σ_{line}, is generally preferred over the FWHM because it is less susceptible to biasing from narrow-line emission and noise (e.g., Peterson et al. 2004).

For completeness, however, we measured the broad emission-line widths in both the mean and the rms spectra, and we report both FWHM and σ_{line}. Before measuring the line widths, we did attempt to subtract the narrow components from the spectra. The [O III] $\lambda 5007$ line was used as a template, and was shifted and scaled to match the narrow components of Hβ, He II, Hγ, and Hδ, as well as additional contaminating narrow-line emission from [S II] $\lambda 4071$ and [O III] $\lambda 4363$. Some residual noise from narrow emission remains in the rms spectrum at the bluest wavelengths, where the intercalibration of the nightly spectra is less accurate (see Figure 3).

Line widths were measured directly from the narrow-line-subtracted spectra, with a local linear continuum defined below each emission line. The uncertainties in the line widths were determined from Monte Carlo random subset sampling, in which N narrow-line-subtracted spectra were selected from the list of N spectra, without regard to whether a spectrum had been previously chosen. The mean and rms spectra were then created from the subset. The local linear continuum beneath an emission line was set by selecting a random region of width at least 15 Å from the total allowed continuum region (typically 50 Å in width, but only 25 Å for the small region between Hβ and He II) on either side of the line, and the FWHM and σ_{line} were then measured and recorded. The process then repeated. This procedure accounts for the effects of including any individual spectrum, with its unique noise properties, in the line-width determination. It further quantifies the uncertainty on the line width from the exact continuum placement. Distributions of the line-width measurements were built up over 1000 realizations, and we report the mean and standard deviation of each distribution as the measurement value and its associated uncertainty.

Finally, we corrected the emission-line widths for the resolution of the spectrograph following Peterson et al. (2004). The measured line width, $\Delta\lambda_{\mathrm{obs}}$, may be described as

$$\Delta\lambda_{\mathrm{obs}}^2 = \Delta\lambda_{\mathrm{true}}^2 + \Delta\lambda_{\mathrm{disp}}^2, \tag{2}$$

where $\Delta\lambda_{\mathrm{true}}$ is the intrinsic line width and $\Delta\lambda_{\mathrm{disp}}$ is the broadening caused by the spectrograph. We adopted the FWHM of [O III] $\lambda5007$ (13.85 Å) as $\Delta\lambda_{\mathrm{obs}}$. The highest-resolution spectrum available for estimating $\Delta\lambda_{\mathrm{true}}$ is the STIS G430M spectrum, which has FWHM = 6.02 Å for [O III] $\lambda5007$. The resolution correction is then $\Delta\lambda_{\mathrm{disp}} \approx 12.5$ Å. In Table 2 we report the final resolution-corrected emission-line widths.

5. Black Hole Mass

The black hole mass is usually determined from reverberation measurements as

$$M_{\mathrm{BH}} = f\frac{c\tau V^2}{G}, \tag{3}$$

where τ is the emission-line time delay, V is the emission-line width, c is the speed of light, and G is the gravitational constant. The factor f is an order-unity scaling factor that accounts for the details of the BLR inclination, geometry, and kinematics. In practice, it is usually not possible to determine the appropriate value of f for each AGN, so a population-averaged value, $\langle f \rangle$, is adopted instead. This "fudge factor" is taken to be the multiplicative factor needed to bring the $M_{\mathrm{BH}}-\sigma_\star$ relationship for AGNs into agreement with the $M_{\mathrm{BH}}-\sigma_\star$ relationship for galaxies with black hole masses determined from dynamical modeling (e.g., Gültekin et al. 2009; Kormendy & Ho 2013; McConnell & Ma 2013). This method should remove any bias from reverberation-based masses on the whole, but results in a factor of 2–3 uncertainty on the mass of any black hole in particular. Typical values of $\langle f \rangle$ range from 2.8 (Graham et al. 2011) to 5.5 (Onken et al. 2004) in the literature depending on the exact sample and the analysis methods, with most investigations settling on values of

$\sim$4–5. Here, we adopt the value of $\langle f \rangle = 4.82$ reported by Batiste et al. (2017), given their careful treatment of morphological effects on measurements of $\sigma_\star$ in the $M_{\mathrm{BH}}-\sigma_\star$ relationship.

Peterson et al. (2004) demonstrated that τ_{cent} combined with σ_{line} produces the least scatter among the predicted masses for NGC 5548, the AGN with the most independent reverberation experiments (14 separate measurements for Hβ at that time). We therefore adopt τ_{cent} for the time delay and σ_{line}(rms) for the line width of Hβ, and the simple prescription in Equation (3) gives a black hole mass of $M_{\mathrm{BH}} = 2.34_{-0.43}^{+0.43} \times 10^7\,M_\odot$ for NGC 3783. If we instead adopt τ_{peak} or τ_{jav} as the Hβ time delay, the predicted mass is consistent within the uncertainties. If FWHM is adopted instead of σ_{line} as the Hβ line-width measurement, then a different value for $\langle f \rangle$ must also be adopted (e.g., Collin et al. 2006), but the predicted mass is again consistent within the uncertainties.

The measurements of the other emission lines presented here may also constrain the black hole mass, but they predict a mass that is lower by $\sim$60%–70%. However, there is reason to be cautious about this result because the use of the [O III] doublet to intercalibrate the spectra means that the ability to quantify real variability in spectral features decreases as the wavelength shifts away from the [O III] lines. The effects of this can be seen in the noisier light curves for Hγ and Hδ and the lower peaks for their CCFs. There are no similar strong and unblended narrow emission lines available to improve the spectral calibration of the region near Hγ and Hδ. This is less of an issue for He II, which is close in wavelength to Hβ and the [O III] doublet; however, it has its own challenges given the low contrast of the emission line relative to the continuum level. The different mass predicted by the properties of the broad He II line could indicate a physical difference between the parts of the BLR that are probed by the two emission lines given their different ionization potentials. If that is the case, then a separate $\langle f \rangle$ would be needed for predicting the black hole mass from the He II emission line.

The black hole mass that we have constrained here is similar to, but slightly smaller than, the mass found by Onken & Peterson (2002) of $M_{\mathrm{BH}} = 2.9_{-0.8}^{+1.1} \times 10^7\,M_\odot$, after scaling their H$\beta$-based mass to account for the difference in adopted $\langle f \rangle$ factors. The improved time sampling in our monitoring program served to decrease the measurement uncertainties, and thus the uncertainties on M_{BH}, by $\sim$50%. Further improvement may be possible but will require moving away from the simplistic mass constraint described above, and instead modeling the full broad-line response as a function of velocity across the emission-line profile (Pancoast et al. 2014; Grier et al. 2017; Williams et al. 2018).

To investigate whether detailed modeling of the Hβ emission-line response may be successful, we defined five relatively equal-width bins across the wavelength (or velocity) range of the line. Two bins were defined for each of the red and blue wings, and one bin was defined for the line center. Light curves for each wavelength bin were then created and their CCFs were determined, following the same procedures as outlined above for the integrated line emission. In Figure 6, we plot the τ_{cent} values for all five wavelength bins, with the Hβ line profile displayed in the bottom panel for reference. The gray horizontal band marks the τ_{cent} range for the emission line as a whole. There is a clear velocity-resolved response across the line profile, with a mostly symmetric shape that has shorter
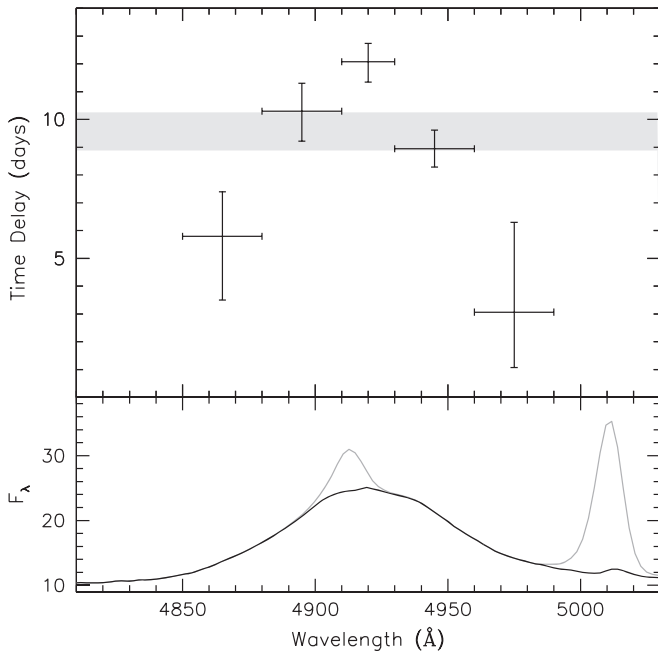
Figure 6. Velocity-resolved time delays (top) across the broad Hβ emission-line profile (bottom). The symmetric response with slightly shorter lags in the red wing of the line is similar to other Seyferts that have been found to have thick disk-like broad-line regions with dynamics that are described by a combination of rotation and inflow.

time delays in the line wings and a longer time delay in the line center. A similar, but weaker, signature is also seen in the He II broad-line response, but the less accurate intercalibration of the spectra at the wavelengths of Hγ and Hδ masks any velocity-resolved response.

For a physically extended and centrally illuminated BLR, the gas that is closest to the outside observer will exhibit the shortest time delays, while the gas that is farthest from the observer will exhibit the longest time delays. While the time delay probes the physical arrangement of the BLR gas, the associated velocity relative to the line center probes the kinematics as viewed by the observer (see Peterson 2001 for a full review). The clear signatures in Hβ and He II are consistent with the expected velocity-resolved response from a rotating disk of broad-line emission, where the time delays measured from redshifted and blueshifted gas would be symmetric around the line center. The shorter time delay in the longest wavelength (most redshifted) bin of Hβ is similar to what has been seen for a few other AGNs, such as Arp 151 (Bentz et al. 2010), where dynamical modeling of the BLR has constrained the gas motions to a combination of rotation and inflow (Pancoast et al. 2014). Given the clear resolution of different time delays across the Hβ emission line, we expect that modeling of the full reverberation response will provide strong constraints on the BLR geometry and kinematics, and thus the black hole mass. Modeling of the broad He II line may allow us to investigate whether there is any evidence for physical differences between the regions of the BLR that are probed by He II versus Hβ. Furthermore, upcoming approved MUSE observations with the Very Large Telescope will allow stellar dynamical modeling to constrain the black hole mass in a completely independent way for direct comparison with the reverberation mass.

6. Summary

We have carried out a successful photometric and spectroscopic monitoring campaign of NGC 3783. Time delays between variations in the continuum and in the broad Hβ, Hγ, Hδ, and He II emission lines are clearly detected. With the reverberation response of the broad Hβ emission line, we constrain a black hole mass of $M_{\rm BH} = 2.34^{+0.43}_{-0.43} \times 10^7 \, M_\odot$. Clear velocity-resolved signatures across the Hβ profile show a symmetric pattern, with shorter lags in the line wings and a longer lag in the line core. Future modeling of the full velocity-resolved response will further constrain the black hole mass and the physical details of the BLR in NGC 3783.

ORCID iDs

Misty C. Bentz ⬤ https://orcid.org/0000-0002-2816-5398
Rachel Street ⬤ https://orcid.org/0000-0001-6279-0552
Christopher A. Onken ⬤ https://orcid.org/0000-0003-0017-349X
Monica Valluri ⬤ https://orcid.org/0000-0002-6257-2341

References

Alard, C. 2000, A&AS, 144, 363
Alard, C., & Lupton, R. H. 1998, ApJ, 503, 325
Barth, A. J., Sarzi, M., Rix, H.-W., et al. 2001, ApJ, 555, 685
Batiste, M., Bentz, M. C., Raimundo, S. I., Vestergaard, M., & Onken, C. A. 2017, ApJL, 838, L10
Bentz, M. C., Denney, K. D., Cackett, E. M., et al. 2006, ApJ, 651, 775
Bentz, M. C., Denney, K. D., Grier, C. J., et al. 2013, ApJ, 767, 149
Bentz, M. C., Horne, K., Barth, A. J., et al. 2010, ApJL, 720, L46
Bentz, M. C., & Manne-Nicholas, E. 2018, ApJ, 864, 146
Bentz, M. C., Peterson, B. M., Netzer, H., Pogge, R. W., & Vestergaard, M. 2009, ApJ, 697, 160
Bessell, M. S. 1999, PASP, 111, 1426
Blandford, R. D., & McKee, C. F. 1982, ApJ, 255, 419
Ciotti, L., Ostriker, J. P., & Proga, D. 2010, ApJ, 717, 708
Collin, S., Kawaguchi, T., Peterson, B. M., & Vestergaard, M. 2006, A&A, 456, 75
Davies, R. I., Thomas, J., Genzel, R., et al. 2006, ApJ, 646, 754
Denney, K. D., Peterson, B. M., Pogge, R. W., et al. 2010, ApJ, 721, 715
Di Matteo, T., Springel, V., & Hernquist, L. 2005, Natur, 433, 604
Dopita, M. A., Shastri, P., Davies, R., et al. 2015, ApJS, 217, 12
Event Horizon Telescope Collaboration, Akiyama, K., Alberdi, A., et al. 2019, ApJL, 875, L6
Ferrarese, L., & Merritt, D. 2000, ApJL, 539, L9
Fischer, T. C., Crenshaw, D. M., Kraemer, S. B., & Schmitt, H. R. 2013, ApJS, 209, 1
Gaskell, C. M., & Peterson, B. M. 1987, ApJS, 65, 1
Gaskell, C. M., & Sparke, L. S. 1986, ApJ, 305, 175
Gebhardt, K., Bender, R., Bower, G., et al. 2000, ApJL, 539, L13
Gebhardt, K., Richstone, D., Tremaine, S., et al. 2003, ApJ, 583, 92
Genzel, R., Pichon, C., Eckart, A., Gerhard, O. E., & Ott, T. 2000, MNRAS, 317, 348

Ghez, A. M., Morris, M., Becklin, E. E., Tanner, A., & Kremenek, T. 2000, Natur, 407, 349
Ghez, A. M., Salim, S., Weinberg, N. N., et al. 2008, ApJ, 689, 1044
Graham, A. W., Onken, C. A., Athanassoula, E., & Combes, F. 2011, MNRAS, 412, 2211
Granato, G. L., De Zotti, G., Silva, L., Bressan, A., & Danese, L. 2004, ApJ, 600, 580
Grier, C. J., Pancoast, A., Barth, A. J., et al. 2017, ApJ, 849, 146
Gültekin, K., Richstone, D. O., Gebhardt, K., et al. 2009, ApJ, 698, 198
Hartman, J. D., Bakos, G., Stanek, K. Z., & Noyes, R. W. 2004, AJ, 128, 1761
Hartman, J. D., Stanek, K. Z., Gaudi, B. S., Holman, M. J., & McLeod, B. A. 2005, AJ, 130, 2241
Henden, A., & Munari, U. 2014, CoSka, 43, 518
Hopkins, P. F., Hernquist, L., Cox, T. J., et al. 2006, ApJS, 163, 1
Kauffmann, G., & Haehnelt, M. 2000, MNRAS, 311, 576
Kormendy, J., & Ho, L. C. 2013, ARA&A, 51, 511
Kourkchi, E., & Tully, R. B. 2017, ApJ, 843, 16
Macchetto, F., Marconi, A., Axon, D. J., et al. 1997, ApJ, 489, 579
Magorrian, J., Tremaine, S., Richstone, D., et al. 1998, AJ, 115, 2285
McConnell, N. J., & Ma, C.-P. 2013, ApJ, 764, 184
Onken, C. A., Ferrarese, L., Merritt, D., et al. 2004, ApJ, 615, 645
Onken, C. A., & Peterson, B. M. 2002, ApJ, 572, 746
Onken, C. A., Valluri, M., Brown, J. S., et al. 2014, ApJ, 791, 37
Pancoast, A., Brewer, B. J., Treu, T., et al. 2014, MNRAS, 445, 3073
Peng, C. Y., Ho, L. C., Impey, C. D., & Rix, H. 2002, AJ, 124, 266
Peng, C. Y., Ho, L. C., Impey, C. D., & Rix, H.-W. 2010, AJ, 139, 2097
Peterson, B. M. 1993, PASP, 105, 247
Peterson, B. M. 2001, in Advanced Lectures on the Starburst-AGN Connection, ed. I. Aretxaga, D. Kunth, & R. Mújica (Singapore: World Scientific), 3
Peterson, B. M. 2010, in IAU Symp. 267, Co-Evolution of Central Black Holes and Galaxies, ed. B. M. Peterson, R. S. Somerville, & T. Storchi-Bergmann (Cambridge: Cambridge Univ. Press), 151
Peterson, B. M., Denney, K. D., De Rosa, G., et al. 2013, ApJ, 779, 109
Peterson, B. M., Ferrarese, L., Gilbert, K. M., et al. 2004, ApJ, 613, 682
Peterson, B. M., Wanders, I., Bertram, R., et al. 1998a, ApJ, 501, 82
Peterson, B. M., Wanders, I., Horne, K., et al. 1998b, PASP, 110, 660
Scannapieco, C., Wadepuhl, M., Parry, O. H., et al. 2012, MNRAS, 423, 1726
Siverd, R. J., Beatty, T. G., Pepper, J., et al. 2012, ApJ, 761, 123
Springel, V., White, S. D. M., Jenkins, A., et al. 2005, Natur, 435, 629
Stirpe, G. M., Winge, C., Altieri, B., et al. 1994, ApJ, 425, 609
Ueda, Y., Hashimoto, Y., Ichikawa, K., et al. 2015, ApJ, 815, 1
van den Bosch, R. C. E. 2016, ApJ, 831, 134
van der Marel, R. P., Cretton, N., de Zeeuw, P. T., & Rix, H.-W. 1998, ApJ, 493, 613
van Groningen, E., & Wanders, I. 1992, PASP, 104, 700
White, R. J., & Peterson, B. M. 1994, PASP, 106, 879
Williams, P. R., Pancoast, A., Treu, T., et al. 2018, ApJ, 866, 75
Zebrun, K., Soszynski, I., & Wozniak, P. R. 2001, AcA, 51, 303
Zu, Y., Kochanek, C. S., & Peterson, B. M. 2011, ApJ, 735, 80